

Influence of microscope settings on dislocation imaging in transmission foreshattered electron imaging (t-FSEI)

Ivan Gutierrez-Urrutia, Akinobu Shibata

Research Center for Structural Materials, National Institute for Materials Science (NIMS), 1-2-1,
Sengen, Tsukuba 305-0047, Japan.

Corresponding author: Ivan Gutierrez-Urrutia

e-mail: gutierrezurrutia.Ivan@nims.go.jp

Phone: +081-29-859-2706

Abstract

This work analyzes the influence of several microscope settings, namely, sample-forescattered electron detector (FSD) distance, and tilting conditions on the characteristics of the dislocation contrast imaged in transmission forescattered electron imaging (t-FSEI). The dislocation contrast behaviors of characteristic dislocation configurations of two Fe-based alloys, namely an α' -martensitic (body-centered cubic, bcc) Fe-33Ni alloy (wt.%), and an austenitic (face-centered cubic, fcc) Fe-30Mn-6.5Al-0.3C alloy (wt.%) were investigated on thin foil samples by using different on-axis transmission Kikuchi diffraction (TKD) configurations, namely t-FSEI, bright-field (BF) t-FSEI and electron channeling contrast imaging (ECCI). The set-ups use transmission Kikuchi electron patterns to orient the crystal into controlled diffraction conditions. Imaging parameters such as dislocation contrast intensity and information depth are analyzed and compared to those obtained in the ECCI mode under the same microscope conditions. These effects are associated with the attenuation of Bragg scattering by high-angle scattering processes and the electron channeling mechanism, respectively. The experimental analysis sets the microscope settings for optimum dislocation imaging in t-FSEI.

Keywords: transmission foreshattered electrons (t-FSE); Electron channeling contrast imaging;

Dislocation imaging; scanning electron microscope (SEM); transmission Kikuchi diffraction

(TKD)

1-Introduction

The imaging of crystal defects in the scanning electron microscope (SEM) is commonly performed by the electron channeling contrast imaging (ECCI) technique [1-10]. ECC images of dislocations are formed by the acquisition of the modulated backscattered electron (BSE) signal associated with the localized lattice plane bending in the vicinity of a dislocation as the incident electron beam is scanned over the sample. Recently, a novel geometry for transmission Kikuchi diffraction (TKD) has been recently introduced (on-axis TKD) [11], where a phosphor screen oriented perpendicular to the incident beam is positioned below an electron transparent sample that is positioned at 0° tilt. The introduction of Si diodes attached to the camera head and placed below the thin foil allows the acquisition of the transmission foreshattered electron (t-FSE) signal produced within the sample [12-15]. Similar to scanning transmission electron microscopy (STEM), t-FSE images with either strong crystallographic orientation contrast (bright-field foreshattered electron ((BF) t-FSE) images) or atomic number contrast (dark-field foreshattered electron ((DF) t-FSE) images) can be formed at small and large collection angles, respectively [12, 14, 16, 17]. Several studies have demonstrated the technical potential of these FSE imaging modes for microstructural characterization at the nano-scale [14, 16-18]. However, the characterization of crystal defects with the t-FSE signal in the SEM has been rather limited. So far, dislocation imaging with the t-FSE signal has been mainly performed by using a STEM detector [19-22]. These works have

demonstrated that dislocations and stacking faults can be characterized on thin foils in the SEM by using the t-FSE signal. In this work, we investigate the influence of several microscope settings, namely, sample-forescattered electron detector (FSD) distance, and tilting conditions on the dislocation contrast behavior imaged in transmission forescattered electron imaging (t-FSEI) by using an on-axis transmission Kikuchi diffraction (TKD) set-up. The dislocation contrast behavior of characteristic dislocation configurations of two Fe-based alloys, namely an α' -martensitic (body-centered cubic, bcc) Fe-33Ni alloy, and an austenitic (face-centered cubic, fcc) Fe-30Mn-6.5Al-0.3C alloy was investigated on thin foil-samples. Controlled diffraction conditions were calculated from the retrieved transmission Kikuchi electron patterns, as in [4, 7]. The influence of the microscope settings on the dislocation contrast was analyzed in terms of the scattering processes contributing to the formation of the t-FSE signal and the dislocation contrast. Imaging parameters such as the information depth and dislocation contrast intensity are analyzed and compared to those obtained in electron channeling contrast imaging (ECCI) under the same microscope conditions.

2-Materials and methods

2.1-Material

Electron channeling contrast (ECC) and transmission foreshattered electron (t-FSE) images of dislocations were acquired on thin foil samples of two Fe-alloys, namely, Fe-33Ni and Fe-30Mn-6.5Al-0.3C (wt.%). The crystal structures of the Fe-33Ni and Fe-30Mn-6.5Al-0.3C alloys are α' -martensitic (body-centered cubic, bcc) and austenitic (face-centered cubic, fcc), respectively. Details of the processing of these alloys can be found in [23, 24]. The thin samples were prepared by two fabrication methods, namely, the twin-jet electrolytic polishing method by using a 10% perchloric acid at room temperature (Fe-33Ni alloy, wt.%) and the in-situ FIB lift-out method on a Scios 2 ThermoFisher Scientific dual-beam SEM system (Fe-30Mn-6.5Al-0.3C alloy, wt.%). Thinning of the FIB lamella was performed at an initial acceleration voltage of 30kV and a milling current of ~ 1000 pA on both sides of the foil followed by a final thinning procedure at 5 kV and 200 pA. The sample thickness at the region of interest of the Fe-33Ni alloy sample was determined using Electron Energy Loss Spectroscopy (EELS) in a JEOL JEM 2800 TEM operating at 200 kV with a convergence angle of 20 mrad and a collection angle of 42 mrad using the log-ratio technique [25]. The estimated sample thickness was 220 ± 10 nm. The size of the lamella fabricated by FIB was about $20 \mu\text{m} \times 20 \mu\text{m} \times 100$ nm. Before imaging, the specimen was plasma-cleaned using an XEI Evactron 25 (XEI Scientific, Inc., Redwood City, USA) de-contaminator. ECCI and t-FSEI were performed on a field emission gun scanning electron microscope (FEG-SEM) Zeiss Sigma (Zeiss, Oberkochen, Germany) equipped with an on-axis transmission Kikuchi diffraction (TKD) system that consists of a Bruker e⁺ Flash^{HD} EBSD (Bruker, Billerica, MA, USA) camera

mounted on a Bruker OPTIMUS™ detector head. The detector head consists of a phosphor screen and three foreshattered electron detectors (FSD) with a size of 5.2 x 4.4 mm² for collecting the transmission foreshattered electron (t-FSE) signal produced within the sample. TKD measurements and ECC/t-FSE images were collected at 30 kV acceleration voltage with an aperture of 60 µm. The microscope was run in the “high current” mode with a probe current of ~ 8.5 nA. Tilting experiments were performed on a 5-axis motorized eucentric stage (x, y, z, tilt, rotation) with an x/y/z step resolution of 1 µm and tilt/rotation step resolution of 0.1°. SEM images were taken at 1024 x 1024 pixels resolution with reduced digital noise (5 minutes per scan).

The SEM set-ups used in this study, namely transmission foreshattered electron imaging (t-FSEI) (a), bright-field (BF) t-FSEI (b), and electron channeling contrast imaging (ECCI) (c), are shown in the sketch of Fig. 1. t-FSE images were acquired by a foreshattered electron detector (FSD) located in the middle of the detector head and placed beneath the thin sample. The (BF) t-FSEI mode corresponds to the acquisition of t-FSE images by placing the FSD normal to the optic axis [14, 17, 26]. In the current SEM configuration, the minimum collection angle α_1 and the maximum collection angle α_2 as a function of the optical axis-FSD distance (DD_2) are defined as:

$$\alpha_1 = \tan^{-1} \left(\frac{DD_2}{DD_1} \right) \quad (1)$$

$$\alpha_2 = \tan^{-1} \left(\frac{DD_2 + a}{DD_1} \right) \quad (2)$$

where DD_1 is the sample-FSD distance along the optical axis ($DD_1 = 18$ mm) and a is the FSD width ($a = 5.2$ mm). The effective collection angle, $\Delta\alpha$, is defined as $\Delta\alpha = \alpha_2 - \alpha_1$. In the ECCI mode (Fig. 1c), ECC images of dislocations were acquired by a solid-state four-quadrant backscattered electron detector (BSED) that collects the BSE signal emitted from the upper surface of the thin foil. The ECCI set-up is characterized by a low-tilt configuration at a 7 mm working distance. The sample-BSED configuration is the same as that used in the conventional EBSD-based ECCI set-up [27, 28]. In the present set-up, the phosphor screen is set underneath the beam to directly acquire transmission Kikuchi electron patterns (TKEPs) of the imaged area. Following the approach described in [4, 27], the Euler angles determined from the collected TKEPs are used to calculate the corresponding electron channeling patterns (ECPs), and hence, the channeling/diffraction conditions used to form the ECC/t-FSE images at a given tilting condition. It is relevant to indicate that the region of the thin foil where TKEPs are formed may be different from that of the formation of the BSE/t-FSE signals. TKEPs are formed in a region of about 10 – 100 nm from the bottom surface of a thin foil [17, 29, 30] whereas BSE/t-FSE signals are typically generated within the whole thickness of a thin foil [31-35]. Accordingly, the on-axis transmission Kikuchi diffraction (TKD) set-ups shown in Fig. 1 are limited to the imaging of dislocations on

thin foils containing a constant crystallographic orientation along the sample thickness. For this, the structural size of the analyzed region along the sample thickness must be considerably larger than the thin foil thickness.

3-Results and discussion

3.1-Effect of detector distance on the dislocation contrast

This section presents the analysis of the effect of the optical axis-FSD distance, DD_2 , on the intensity of the dislocation contrast imaged by the transmission forescattered electron signal (t-FSE). Fig. 2 shows a series of t-FSE images of dislocations taken at different values of DD_2 corresponding to a range of maximum collection angle, α_2 , between 140 mrad and 815 mrad. Ranges of maximum and minimum collection angles, α_1 and α_2 , calculated with equations (1) and (2) for different values of DD_2 are shown in Table 1. The t-FSE images were acquired on a thin-foil sample of a Fe-33Ni alloy (thickness of 220 ± 10 nm) and taken under two-beam diffraction conditions using the diffraction vector (2 1 1) with $w > 0$ (w : deviation parameter). As a comparison, the (BF) t-FSE image taken with $\alpha_2 = 145$ mrad is shown in Fig. 2(a). The series of t-FSE images reveal two main characteristics, namely, the visibility of the dislocation contrast within a large range of α_2 (~ 785 mrad), and the attenuation of the intensity of the dislocation contrast with the

detector distance, and hence α_2 . Specifically, when $\alpha_2 < 500$ mrad, dislocations exhibit a strong contrast characterized by a dark sharp contrast over a bright background similar to that imaged in (BF)-TEM. When $\alpha_2 > 500$ mrad, the dislocation contrast becomes weaker and vanishes at $\alpha_2 \sim 815$ mrad. This effect is analyzed in Fig. 3. This figure plots the variation of the transmitted electron yield, TEY, (ratio of the number of collected transmitted electrons by the total number of electrons), dislocation contrast intensity, I_{dc} , and intensity of the t-FSE signal of the matrix, I_{matrix} , as a function of α_2 . TEY was calculated from the Monte Carlo simulations of electron trajectories produced by scattering elastic scattering and inelastic events approximated by a mean energy loss model between two elastic scattering events by the software Casino version 3.3 [36-38]. The simulations were obtained for an accelerating voltage of 30 kV and a beam diameter of 3 nm, which is approximately equal to that used experimentally. One million electron trajectories were simulated to decrease the statistical variation inherent in the Monte Carlo method. I_{dc} was measured from the intensity profile measured across the dislocation line indicated by an arrow in Fig. 2. I_{dc} is defined as $I_{dc} = (I_{max} - I_{min}) / (I_{max} + I_{min})$, where I_{max} and I_{min} correspond to the highest and lowest values of the intensity profile of the t-FSE signal across a dislocation. I_{matrix} is estimated as the average value of the pixel intensity of a matrix region free of dislocations.

Fig. 3 shows that the experimentally determined attenuation of I_{matrix} with α_2 follows a similar trend to the variation of TEY with α_2 calculated by Monte Carlo simulations. This means that the total number of collected foreshattered electrons decreases with the optical axis-FSD distance (DD_2) and hence, the intensity of the t-FSE signal is attenuated. Interestingly, the variation of I_{dc} with α_2 reveals several features of the influence of the detector distance on the dislocation contrast. The present results indicate that in the current configuration ($DD_1 = 18$ mm), a strong dislocation contrast ($I_{dc} \sim 0.10 - 0.15$) is imaged on t-FSE images by placing the FSD at a small optical axis-FSD distance, DD_2 , between 0 mm (BF-mode) and 4 mm. It corresponds to a maximum collection angle range (α_2) of 525 mrad. With increasing DD_2 , the dislocation contrast becomes weaker ($I_{dc} < 0.10$ for $525 < \alpha_2 < 785$ mrad) and it vanishes at $DD_2 = 14$ mm ($\alpha_2 > 815$ mrad). The observed dependence of the dislocation contrast on the detector distance can be qualitatively explained as follows. The collected t-FSE signal consists of small-angle scattered electrons (Bragg scattering) and high-angle scattered electrons (Rutherford scattering and thermal diffuse scattering) [39]. At small values of α_2 , the diffracted signal strongly contributes to the collected t-FSE signal resulting in a strong dislocation contrast. At increased values of α_2 , the t-FSE signal is gradually formed by high-angle scattered electrons due to the attenuation of Bragg scattering by thermal vibrations. At large values of α_2 , the t-FSE signal is dominated by thermal diffuse scattered electrons and exhibits a Z^2 -dependence (Z-contrast) [40-42]. Several works have reported Z-contrast on t-FSE images

acquired at large collection angles [12, 26]. The angular dependences of the scattering processes contributing to the t-FSE signal results in the attenuation of I_{dc} with α_2 resulting in a gradual smearing out of the dislocation contrast. This effect has been reported on a thin foil sample of a Zr alloy containing Nb particles using a similar on-axis transmission Kikuchi diffraction (TKD) configuration than that shown in Fig. 1(a) [26]. This study shows that under similar microscope conditions to those used in the present study, diffraction contrast vanishes at large maximum collection angles ($\alpha_2 > 760$ mrad). According to Jesson and Pennycook [43, 44], the minimum collection angle for Z-contrast scales with $\lambda/\Delta R$, where λ is the electron wavelength and ΔR is the distance between neighboring atomic columns. The smaller α_2 reported in the Zr sample where diffraction contrast vanishes (Zr: $\alpha_2 > 760$ mrad; Fe33-Ni: $\alpha_2 > 815$ mrad) can be associated with the larger atomic plane spacing of the Zr sample used to form the t-FSE images.

3.2-Influence of channeling conditions on the dislocation contrast

The influence of channeling conditions on the intensity of the dislocation contrast was evaluated on (BF) t-FSE images of the deformation band (DB) structure of a Fe-30Mn-6.5Al-0.3C alloy (wt.%) deformed at -196 °C. The deformation band structure is formed by an inhomogeneous deformation process, as described in [23]. Fig. 4 shows two examples showing the effect of the

deviation parameter, w , on the dislocation contrast of the dislocation configuration of a deformation band displayed on ECC images (a, c) and the corresponding (BF) t-FSE images (b, d) taken under two-beam conditions using the diffraction vector (2 4 0). ECC/(BF) t-FSE images (a, b) and (c, d) were taken under $w < 0$ and $w > 0$ channeling/diffraction conditions, respectively. The diffraction conditions were set by tracking the modulation of the BSE signal with w , as in [4]. Due to the low intensity of the BSE signal produced by the thin sample (BSE yield is strongly dependent on the sample thickness), dislocation contrast is only visible on the (BF) t-FSE images. In a thicker thin-foil (thickness of ~ 220 nm), dislocation contrast is visible on a ECC image (Fig. 6(b)). The deformation band (DB) is characterized by a localized dislocation configuration of ~ 1.5 μm wide that is formed by closely spaced dislocation configurations lying on non-coplanar $\{111\}$ slip systems. The dislocation configuration is visible as dark compact layers over a bright background. The deformation band is delimited by a boundary region of about $0.2 - 0.4$ μm wide containing a high localized plastic deformation.

The ECC/(BF) t-FSE images reveal a strong channeling effect on the intensity of the BSE/t-FSE signal. As expected, the ECC images exhibit a strong dependence of the BSE signal on the deviation parameter, w , which is associated with the channeling mechanism [4, 45]. Interestingly, the (BF) t-FSE images also reveal a strong channeling effect on the intensity of the t-FSE signal.

Fig. 5 plots the intensity profiles of the t-FSE signal measured across the same dislocation

configuration (indicated by an arrow in Fig. 4) imaged under $w > 0$ and $w < 0$ conditions, respectively. The width of the dislocation configuration (measured from the width of the profile at half peak height) estimated from both profiles is similar, i.e. about 65 nm. However, under $w > 0$ conditions, the t-FSE signal associated with the crystal matrix, I_{t-FSE}^{matrix} , exhibits a stronger intensity ($I_{t-FSE}^{matrix} = 175 \pm 25$ (gray value)) than that under $w < 0$ conditions ($I_{t-FSE}^{matrix} = 75 \pm 10$ (gray value)), Figs. 4(b, d). As the intensity of the t-FSE signal associated with the dislocation configuration is roughly constant under the current channeling conditions, the channeling effect results in an enhanced dislocation contrast. Defining the dislocation contrast intensity, I_{dc} , as $I_{dc} = (I_{t-FSE}^{matrix} - I_{t-FSE}^{dis}) / (I_{t-FSE}^{matrix} + I_{t-FSE}^{dis})$, where I_{t-FSE}^{matrix} and I_{t-FSE}^{dis} correspond to the average intensities of the t-FSE signal of the crystal matrix and that of the matrix region containing a dislocation, respectively, it yields $I_{dc} = 0.45$ ($w > 0$) and $I_{dc} = 0.3$ ($w < 0$). The present findings indicate that channeling effects play a significant effect in the intensity of the dislocation contrast in (BF)-tFSEI. The observed channeling effect is similar to that occurring on the forward-scattered beam in TEM [46-48]. The effect is associated with the inelastic and incoherent scattering of the transmitted FSE signal as the primary beam travels along the lattice crystal (channeling mechanism), resulting in the modulation of the t-FSE signal with the deviation parameter, w . The effect of w on the t-FSE signal is reverted to that on the BSE signal due to the characteristic modulation of the BSE/t-FSE signals with w . The channeling effect is expected to be visible in thick samples (thickness > 100 nm) and contributes to the intensity of the dislocation contrast displayed on (BF) t-FSE images.

3.3-Information depth

As ECCI is a relevant SEM imaging mode of dislocations, we have comparatively analyzed the information depths in (BF) t-FSEI and ECCI on a thin sample of Fe-33Ni alloy (wt.%) (sample thickness of 220 ± 10 nm). The information depths were analyzed through the comparison of the dislocation contrast imaged by (BF) t-FSEI and ECCI under the same channeling conditions. (BF) t-FSE and ECC images were acquired by the set-ups shown in Fig. 1(b) and Fig. 1(c), respectively. Fig. 6 shows an example of a (BF) t-FSE image (a) and an ECC image (b) of the dislocation configuration in the interior of a α' martensite plate taken under two-beam diffraction conditions using the diffraction vector $(-2\ 1\ 1)$, with $w > 0$. The images display a projection of two sets of dislocation lines. Most of the dislocation lines are straight and a few curved dislocation lines are visible, which indicates the presence of a local stress field. Considering the bcc-structure of α' martensite, the observed dislocations correspond to $\langle 111 \rangle$ -type screw dislocations [24]. Accordingly, the Burgers vector is parallel to the dislocation line direction. As expected, the dislocation contrast displayed on the (BF) t-FSE image is inverted to that shown on the ECC image, as shown in the intensity profiles of Figs. 6(c), 6(d). These plots were acquired across the same dislocation line (indicated by an arrow in Figs. 6(a), 6(b)). Although the absolute value of the dislocation contrast intensity displayed on these images can not be compared due to the different

detector settings that influence the absolute intensity value [31], the reversion of the contrast is measurable. The plots also show that the dislocation feature width, y , imaged on the (BF) t-FSE/ECC images is similar ($y \sim 31$ nm measured on the (BF) t-FSE image; $y \sim 33$ nm measured on the ECC image).

Fig. 7 shows the analysis of the visible dislocation lines imaged on the (BF) t-FSE image and ECC image. Blue lines correspond to dislocation lines that are imaged in the same configuration in both imaging modes. Red lines correspond to dislocation lines that are imaged in a different dislocation configuration. The analysis reveals that the dislocation configuration imaged in the two imaging modes is nearly identical. Only a few dislocation lines were imaged in a slightly different configuration. The analysis indicates that in the analyzed thin foil, the dislocation contrast displayed in both imaging modes, i.e. (BF) t-FSEI and ECCI, originates within the same sample thickness. As the t-FSE signal is generated within the whole sample thickness, it suggests that under the current microscope conditions, the ECCI information depth, d_{ECCI} , is at least the thickness of the analyzed area, i.e. $d_{ECCI} > 220 \pm 10$ nm. d_{ECCI} of a given material can be estimated by the estimation of the attenuation of the intensity of the primary electron Bloch wave when traveling through a crystal [49]. It yields $d_{ECCI} \sim 5 \xi_g$, where ξ_g is the extinction distance for a given diffraction vector and electron beam energy. This approach has been used to estimate d_{ECCI} at acceleration voltages of 20 – 30 kV in polycrystalline materials containing crystal defects [2, 5,

22, 50, 51]. Under the current $(-2\ 1\ 1)$ channeling conditions, $\xi_{211} \sim 50$ nm for bcc-Fe at 100 KeV [47, 48]). Assuming an energy correction where the ratio of the relativistic factors is considered [47], we obtain $\xi_{211} \sim 45$ nm, and hence, $d_{ECCI} \sim 225$ nm. This value agrees with the range of d_{ECCI} experimentally determined from the observations of the dislocation configurations. Accordingly, our analysis indicates that in the present thin-foil sample and under the current microscope conditions, the ECCI information depth, d_{ECCI} , is the same as the t-FSEI information depth, d_{t-FSEI} , resulting in an identical imaged dislocation configuration (same number of visible dislocation lines and similar dislocation feature width) that is displayed with a comparatively reverted contrast. However, if the ECC images are formed using a diffraction vector with small ξ_g (for instance, $\xi_{110} \sim 25$ nm for bcc-Fe at 100 KeV), $d_{ECCI} < d_{t-FSEI}$ and hence, the dislocation configuration displayed on ECC images will be different to that displayed on the corresponding (BF) t-FSEI images taken under the same diffraction conditions. This effect may be useful for understanding 3D effects on the dislocation configuration imaged in ECCI and (BF) t-FSEI.

4-Conclusions

This work analyzes the influence of several microscope settings, namely, sample-forescattered electron detector (FSD) distance, and tilting conditions on the dislocation contrast behavior in transmission foreshattered electron imaging (t-FSEI). These effects were investigated on the

dislocation configuration of thin-foil samples of two Fe-based alloys, namely an α' -martensitic (body-centered cubic, bcc) Fe-33Ni alloy (wt.%), and an austenitic (face-centered cubic, fcc) Fe-30Mn-6.5Al-0.3C alloy (wt.%) on several on-axis transmission Kikuchi diffraction (TKD) set-ups. The following conclusions can be drawn:

-The optical axis-FSD distance, DD_2 , has a strong influence on the intensity of the dislocation contrast imaged in t-FSEI. In the current microscope set-up, a strong dislocation contrast ($I_{dc} \sim 0.10 - 0.15$) is imaged on t-FSE images by placing the FSD at a small optical axis-FSD distance, DD_2 , between 0 mm (BF-mode) and 4 mm. With increasing DD_2 , the dislocation contrast becomes weaker ($I_{dc} < 0.10$ for $525 < \alpha_2 < 785$ mrad) and it vanishes at $DD_2 = 14$ mm ($\alpha_2 > 815$ mrad). This effect is attributed to the attenuation of Bragg scattering by high-angle scattering processes resulting in the attenuation of the dislocation contrast with α_2 .

-Channeling effects play a significant role in the dislocation contrast intensity in (BF) t-FSEI. We find that the dislocation contrast intensity enhances under $w > 0$ conditions. This effect is associated with the channeling effect generated as the primary beam travels along the lattice crystal resulting in a modulated t-FSE signal. Comparatively, the influence of the channeling effect on the t-FSE signal is reverted to that on the BSE signal due to the characteristic modulation of the BSE and t-FSE signals with the deviation parameter, w .

-Experimental determinations of the ECCI information depth, d_{ECCI} , and t-FSEI information depth, d_{t-FSEI} , through the analysis of the imaged dislocation configuration show that under specific microscope conditions ((2 1 1) diffraction conditions and 30 kV), $d_{ECCI} = d_{t-FSEI}$. This results in an identical imaged dislocation configuration (same number of visible dislocation lines and similar dislocation feature width) that is displayed with a comparatively reverted contrast. We expect that under diffraction conditions where the extinction distance is small (for instance, $\xi_{110} \sim 25$ nm for bcc-Fe at 100 KeV), the dislocation configuration imaged in ECCI will be different from that displayed in the corresponding (BF) t-FSE image. This effect may be useful for understanding 3D effects on the dislocation configuration imaged in ECCI and (BF) t-FSEI.

Acknowledgments

This study was financially supported by a project commissioned by the New Energy and Industrial Technology Development Organization (NEDO) [JPNP14014].

References

- [1] H. Mansour, J. Guyon, M.A. Crimp, N. Gey, B. Beausir, N. Maloufi, Accurate electron channeling contrast analysis of dislocations in fine grained bulk materials, *Scripta Mater.* 84-85 (2014) 11-14. <https://doi.org/10.1016/j.scriptamat.2014.03.001>.
- [2] I. Gutierrez-Urrutia, Analysis of dislocation configurations in a [0 0 1] fcc single crystal by electron channeling contrast imaging in the SEM, *Microscopy* 66 (2017) 63-67. <https://doi.org/10.1093/jmicro/dfw099>.
- [3] H. Kriaa, A. Guitton, N. Maloufi, Fundamental and experimental aspects of diffraction for characterizing dislocations by electron channeling contrast imaging in scanning electron microscope, *Sci. Rep.* 7 (2017) 9742. <https://doi.org/10.1038/s41598-017-09756-3>.
- [4] I. Gutierrez-Urrutia, Quantitative analysis of electron channeling contrast of dislocations, *Ultramicroscopy* 206 (2019) 112826. <https://doi.org/10.1016/j.ultramic.2019.112826>.
- [5] B. Pang, I.P. Jones, Y.-L. Chiu, J.C.F. Millett, G. Whiteman, Electron channelling contrast imaging of dislocations in a conventional SEM, *Phil. Mag* 97 (2017) 346-359. <https://doi.org/10.1080/14786435.2016.1262971>.
- [6] M. Feifel, J. Ohlmann, R.M. France, D. Lackner, F. Dimroth, Electron channeling contrast imaging investigation of stacking fault pyramids in GaP on Si nucleation layers, *J. Crystal Growth* 532 (2020) 125422.
- [7] I. Gutierrez-Urrutia, Analysis of electron channeling contrast of stacking faults in fcc materials, *Micros. Microanal.* 27 (2021) 318-325. <https://doi.org/10.1017/S1431927620024952>.

- [8] G. Naresh-Kumar, D. Thomson, Y. Zhang, J. Bai, L. Jiu, X. Yu, Y.P. Gong, R.M. Smith, T. Wang, C. Trager-Cowan, Imaging basal plane stacking faults and dislocations in (11-22) GaN using electron channelling contrast imaging, *J. Appl. Phys.* 124 (2018) 065301. <https://doi.org/10.1063/1.5042515>.
- [9] B.E. Dunlap, T.J. Ruggles, D.T. Fullwood, B. Jackson, M.A. Crimp, Comparison of dislocation characterization by electron channeling contrast imaging and cross-correlation electron backscattered diffraction, *Ultramicroscopy* 184 (2018) 125-133.
- [10] A. Weidner, H. Biermann, Case studies on the application of high-resolution electron channelling contrast imaging – investigation of defects and defect arrangements in metallic materials, *Phil. Mag* 95 (2017) 759-793.
- [11] J.J. Funderberger, E. Bouzy, D. Goran, J. Guyon, H. Yuan, A. Morawiec, Orientation mapping by transmission-SEM with an on-axis detector, *Ultramicroscopy* 161 (2016) 17-22.
- [12] N. Brodusch, H. Demers, R. Gauvin, Dark-Field Imaging of Thin Specimens with a Forescatter Electron Detector at Low Accelerating Voltage, *Microsc. Microanal.* 19 (2013) 1688-1697. <https://doi.org/10.1017/S1431927613013287>.
- [13] W. Zielinski, T. Plocinski, K.J. Kurzydowski, Transmission Kikuchi diffraction and transmission electron forescatter imaging of electropolished and FIB manufactured TEM specimens, *Mater. Charact.* 104 (2015) 42-48. <https://doi.org/10.1016/j.matchar.2015.04.003>.
- [14] A.B.S. Fanta, A. Fuller, H. Alimadadi, M. Todeschini, D. Goran, A. Burrows, Improving the imaging capability of an on-axis transmission Kikuchi detector, *Ultramicroscopy* 206 (2019) 112812. <https://doi.org/10.1016/j.ultramic.2019.112812>.

- [15] C. Ernould, B. Beausir, J.-J. Fundenberger, V. Taupin, E. Bouzy, Characterization at high spatial and angular resolutions of deformed nanostructures by on-axis HR-TKD, *Scripta Mater.* 185 (2020) 30-35. <https://doi.org/10.1016/j.scriptamat.2020.04.005>.
- [16] P.W. Trimby, Y. Cao, Z. Chen, S. Han, K.J. Hemker, J. Lian, X. Liao, P. Rottmann, S. Samudrala, J. Sun, J.T. Wang, J. Wheeler, J.M. Cairney, Characterizing deformed ultrafine-grained and nanocrystalline materials using transmission Kikuchi diffraction in a scanning electron microscope, *Acta Mater.* 62 (2014) 69-80. <https://doi.org/10.1016/j.actamat.2013.09.026>.
- [17] J. Liu, S. Lozano-Perez, A.J. Wilkinson, C.R.M. Grovenor, On the depth resolution of transmission Kikuchi diffraction (TKD) analysis, *Ultramicroscopy* 205 (2019) 5-12. <https://doi.org/10.1016/j.ultramic.2019.06.003>.
- [18] E. Brodu, S.D. Jadhav, K. Vanmeensel, M. Seefeldt, Determination of the structure and orientation of nanometer-sized precipitates in matrix materials via transmission diffraction signals emitted by bulk samples in the Scanning Electron Microscope, *Mater. Charact.* 166 (2020) 110454.
- [19] C. Sun, E. Müller, M. Meffert, D. Gerthsen, Analysis of crystal defects by scanning transmission electron microscopy (STEM) in a modern scanning electron microscope, *Adv Struct Chem Imag* 5 (2019) 1. <https://doi.org/10.1186/s40679-019-0065-1>.
- [20] P.G. Callahan, J.-C. Stinville, E.R. Yao, M.P. Echlin, M.S. Titus, M.D. Graef, D.S. Gianola, T.M. Pollock, Transmission scanning electron microscopy: Defect observations and image simulations, *Ultramicroscopy* 186 (2018) 49-61. <https://doi.org/10.1016/j.ultramic.2017.11.004>.
- [21] J.C. Stinville, E.R. Yao, P.G. Callahan, J. Shin, F. Wang, M.P. Echlin, T.M. Pollock, D.S. Gianola, Dislocation dynamics in a nickel-based superalloy via in-situ transmission scanning electron microscopy, *Acta Cryst.* 168 (2019) 152-166.

- [22] H. Han, L. Strakos, T. Hantschel, C. Porret, T. Vystavel, R. Loo, M. Caymax, Crystalline defect analysis in epitaxial Si_{0.7}Ge_{0.3} layer using site-specific ECCI-STEM, *Micron* 150 (2021) 103123. <https://doi.org/10.1016/j.micron.2021.103123>.
- [23] I. Gutierrez-Urrutia, A. Shibata, K. Tsuzaki, Microstructural study of microbands in a Fe-30Mn-6.5Al-0.3C low-density steel deformed at cryogenic temperature by combined electron channeling contrast imaging and electron backscatter diffraction, *Acta Mater.* 233 (2022) 117980. <https://doi.org/10.1016/j.actamat.2022.117980>.
- [24] A. Shibata, S. Morito, T. Furuhashi, T. Maki, Substructures of lenticular martensites with different martensite start temperatures in ferrous alloys, *Acta Mater.* 57 (2009) 483–492. <https://doi.org/10.1016/j.actamat.2008.09.030>.
- [25] T. Malis, S. Cheng, R. Egerton, EELS log ratio technique for specimen-thickness measurement in the TEM, *J. Electron Microsc. Tech.* 8 (1988) 193-200. <https://doi.org/10.1002/jemt.1060080206>.
- [26] J. Liu, S. Lozano-Perez, P. Karamched, J. Holter, A.J. Wilkinson, C.R.M. Grovenor, Fore-scattered electron imaging of nanoparticles in a scanning electron microscopy, *Mater. Charact.* 155 (2019) 109814.
- [27] I. Gutierrez-Urrutia, S. Zaefferer, D. Raabe, Electron channeling contrast imaging of twins and dislocations in twinning-induced plasticity steels under controlled diffraction conditions in a scanning electron microscope, *Scripta Mater.* 61 (2009) 737-740. <https://doi.org/10.1016/j.scriptamat.2009.06.018>.
- [28] I. Gutierrez-Urrutia, S. Zaefferer, D. Raabe, Coupling of electron channeling with EBSD: toward the quantitative characterization of deformation structures in the SEM, *JOM* 65 (2013) 1229-1236. <https://doi.org/10.1007/s11837-013-0678-0>.

- [29] E. Brodu, E. Bouzy, Depth Resolution Dependence on Sample Thickness and Incident Energy in On-Axis Transmission Kikuchi Diffraction in Scanning Electron Microscope (SEM), *Microsc. Microanal.* 23 (2017) 1096-1106. <https://doi.org/10.1017/S1431927617012697>.
- [30] R.v. Bremen, D.R. Gomes, L.T.H.d. Jeer, V. Ocelík, J.T.M.D. Hosson, On the optimum resolution of transmission-electron backscattered diffraction (t-EBSD), *Ultramicroscopy* 160 (2016) 256-264. <https://doi.org/10.1016/j.ultramic.2015.10.025>.
- [31] L. Reimer, *Scanning Electron Microscopy*, Springer-Verlag, Berlin, 1985.
- [32] R.F. Egerton, *Physical Principles of Electron Microscopy. An Introduction to TEM, SEM, and AEM*, 2005.
- [33] J. Pinos, S. Mikmekova, L. Frank, About the information depth of backscattered electron imaging, *J. Microsc.* 266 (2017) 335-342.
- [34] W. Wisniewski, S. Saager, A. Böbenroth, C. Rüssel, Experimental evidence concerning the significant information depth of electron backscatter diffraction (EBSD), *Ultramicroscopy* 173 (2017) 1-9.
- [35] J.A. Österreicher, F. Grabner, A. Schiffl, S. Schwarz, G.R. Bourret, Information depth in backscattered electron microscopy of nanoparticles within a solid matrix, *Mater. Charact.* 138 (2018) 145-153.
- [36] P. Hovington, D. Drouin, R. Gauvin, CASINO: A new Monte Carlo code in C language for electron beam interaction—Part I: Description of the program, *Scanning* 19 (1997) 1-14. <https://doi.org/10.1002/sca.4950190101>.
- [37] D. Drouin, A.R. Couture, D. Joly, X. Tastet, V. Aimez, R. Gauvin, CASINO V2.42: a fast and easy-to-use modeling tool for scanning electron microscopy and microanalysis users, *Scanning* 29 (2007) 92-101. <https://doi.org/10.1002/sca.20000>.

- [38] H. Demers, N. Poirier-Demers, A.R. Couture, D. Joly, M. Guilmain, N.d. Jonge, D. Drouin, Three-dimensional electron microscopy simulation with the CASINO Monte Carlo software, *Scanning* 33 (2011) 135-146. <https://doi.org/10.1002/sca.20262>.
- [39] S. Pennycook, Z-contrast STEM for materials science, *Ultramicroscopy* 30 (1989) 58-69. [https://doi.org/10.1016/0304-3991\(89\)90173-3](https://doi.org/10.1016/0304-3991(89)90173-3).
- [40] E.J. Kirkland, R.F. Loane, J. Silcox, Simulation of annular dark field STEM images using a modified multislice method, *Ultramicroscopy* 23 (1987) 77-96. [https://doi.org/10.1016/0304-3991\(87\)90229-4](https://doi.org/10.1016/0304-3991(87)90229-4)
- [41] S. Hillyard, J. Silcox, Detector geometry, thermal diffuse scattering and strain effects in ADF STEM imaging, *Ultramicroscopy* 58 (1995) 6-17. [https://doi.org/10.1016/0304-3991\(94\)00173-K](https://doi.org/10.1016/0304-3991(94)00173-K).
- [42] R. Loane, P. Xu, J. Silcox, Incoherent imaging of zone axis crystals with ADFSTEM, *Ultramicroscopy* 40 (1992) 121-138. [https://doi.org/10.1016/0304-3991\(92\)90054-N](https://doi.org/10.1016/0304-3991(92)90054-N)
- [43] D. Jesson, S.J. Pennycook, Incoherent imaging of crystals using thermally scattered electrons, *Proc. R. Soc. A* 449 (1995) 273-293.
- [44] D. Jesson, S.J. Pennycook, Incoherent imaging of thin specimens using coherently scattered electrons, *Proc. R. Soc. A* 441 (1993) 261-281.
- [45] D.C. Joy, D.E. Newbury, D.L. Davidson, Electron channeling patterns in the scanning electron microscope, *Rev. Phys. Appl.* 53 (1982) 81-122.
- [46] D.B. Williams, C.B. Carter, *Transmission Electron Microscopy. A Textbook for Materials Science*, Springer, 2009.
- [47] B. Fultz, J.M. Howe, *Transmission Electron Microscopy and Diffractometry of Materials*, Springer-Verlag, 2013.

- [48] L. Reimer, H. Kohl, Transmission Electron Microscopy. Physics of Image Formation, 5th ed., Springer, 2008.
- [49] A.J. Wilkinson, G.R. Anstis, J.T. Czernuszka, N.J. Long, P.B. Hirsch, Electron channelling contrast imaging of interfacial defects in strained silicon-germanium layers on silicon, *Phil. Mag A* 68 (1993) 59-80. <https://doi.org/10.1080/01418619308219357>.
- [50] I. Gutierrez-Urrutia, D. Raabe, Dislocation density measurement by electron channeling contrast imaging in a scanning electron microscope, *Scripta Mater.* 66 (2012) 343-346. <https://doi.org/10.1016/j.scriptamat.2011.11.027>.
- [51] S. Zaefferer, N.-N. Elhami, Overview No. 154. Theory and application of electron channelling contrast imaging under controlled diffraction conditions, *Acta Mater.* 75 (2014) 20–50. <https://doi.org/10.1016/j.actamat.2014.04.018>.

Table 1. Values of α_1 (minimum collection angle), α_2 (maximum collection angle), and $\Delta\alpha$ (effective collection angle) as a function of DD_2 (detector distance).

DD_2 (mm)	0	4	6	8	10	12	14
α_1 (mrad)	-140	220	320	420	510	615	660
α_2 (mrad)	140	475	555	625	695	785	815
$\Delta\alpha$ (mrad)	280	250	235	205	185	170	155

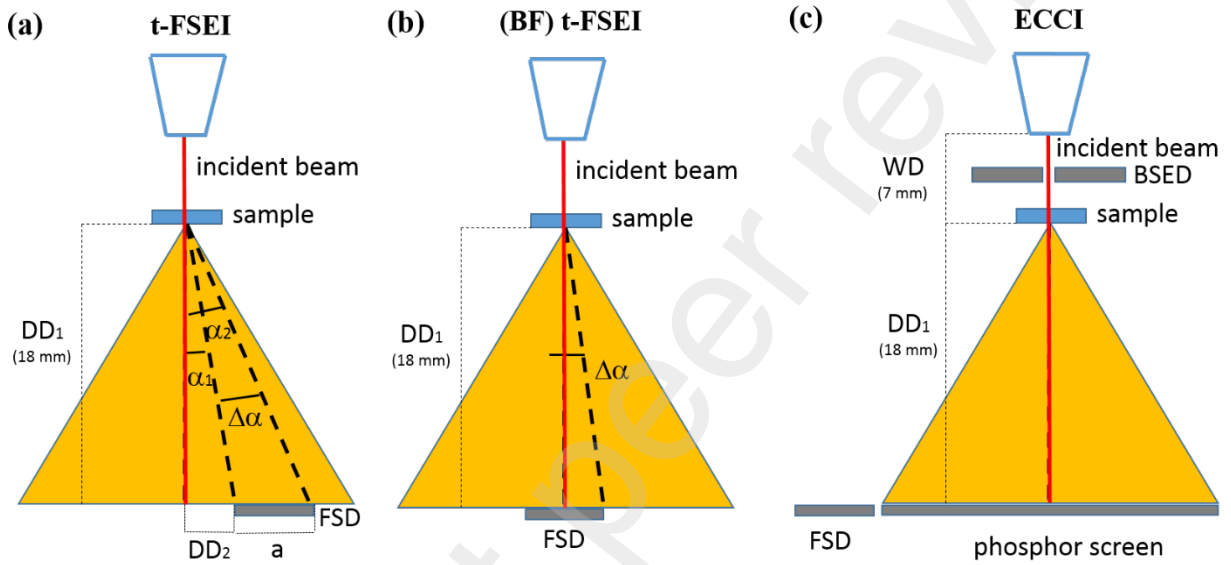


Figure 1. Schematic of the SEM set-ups. (a): Transmission foreshattered electron imaging (t-FSEI); (b): Bright-field transmitted foreshattered electron imaging ((BF) t-FSEI); (c): Electron channeling contrast imaging (ECCI). DD_1 : sample-FSD distance along the optical axis. DD_2 : detector distance. a : FSD width. α_1 : minimum collection angle. α_2 : maximum collection angle. $\Delta\alpha$: effective collection angle. BSED: backscattered electron detector. FSED: foreshattered electron detector.

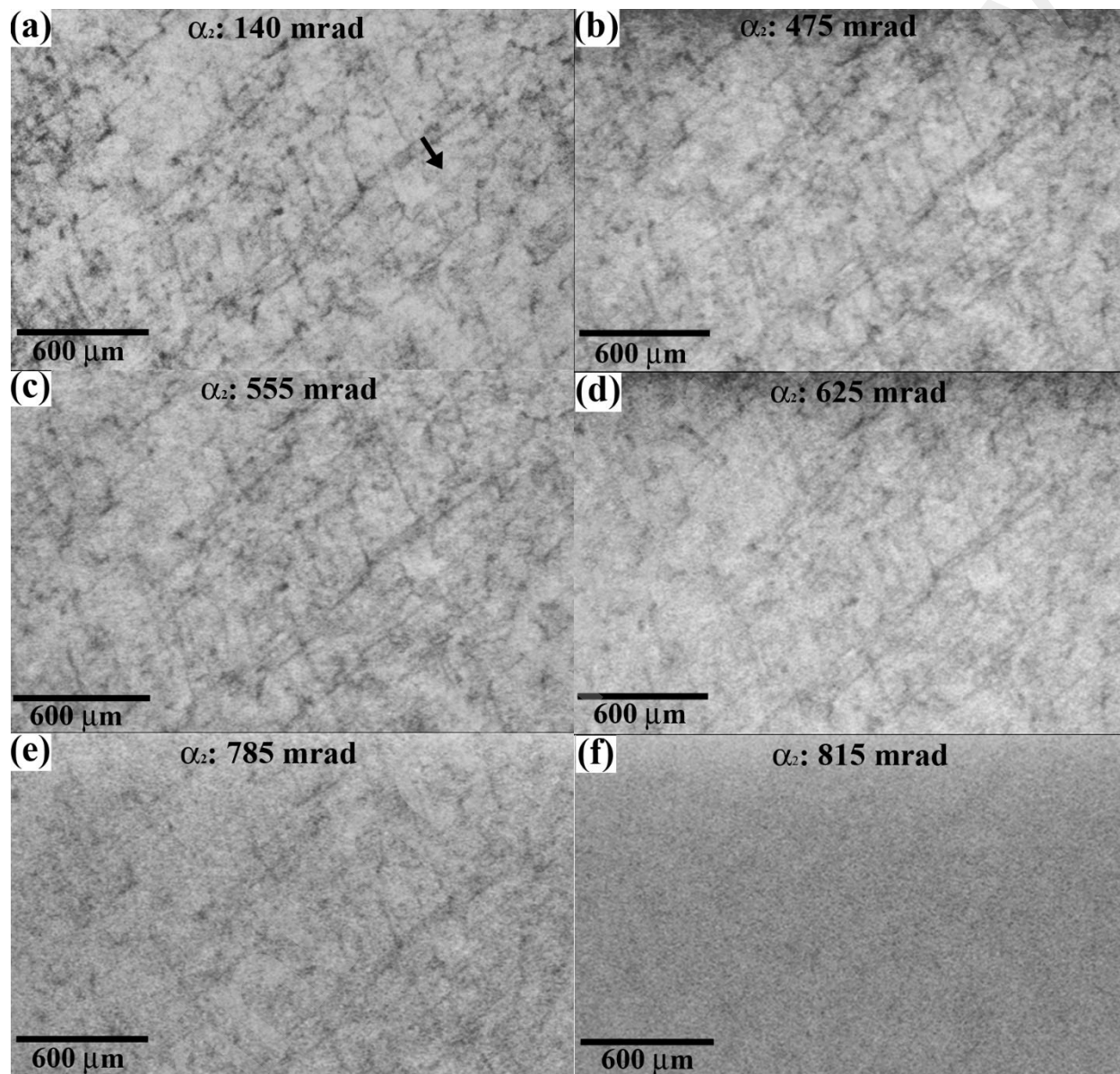


Figure 2. Influence of the maximum collection angle (α_2) on the dislocation contrast imaged in t-FSEI using the set-up shown in Fig. 1(a). The t-FSEI images were collected on a thin foil of a Fe-33Ni alloy (thickness of 220 ± 10 nm) and taken under two-beam diffraction conditions using $g(2\ 1\ 1)$ with $w > 0$ (w : deviation parameter).

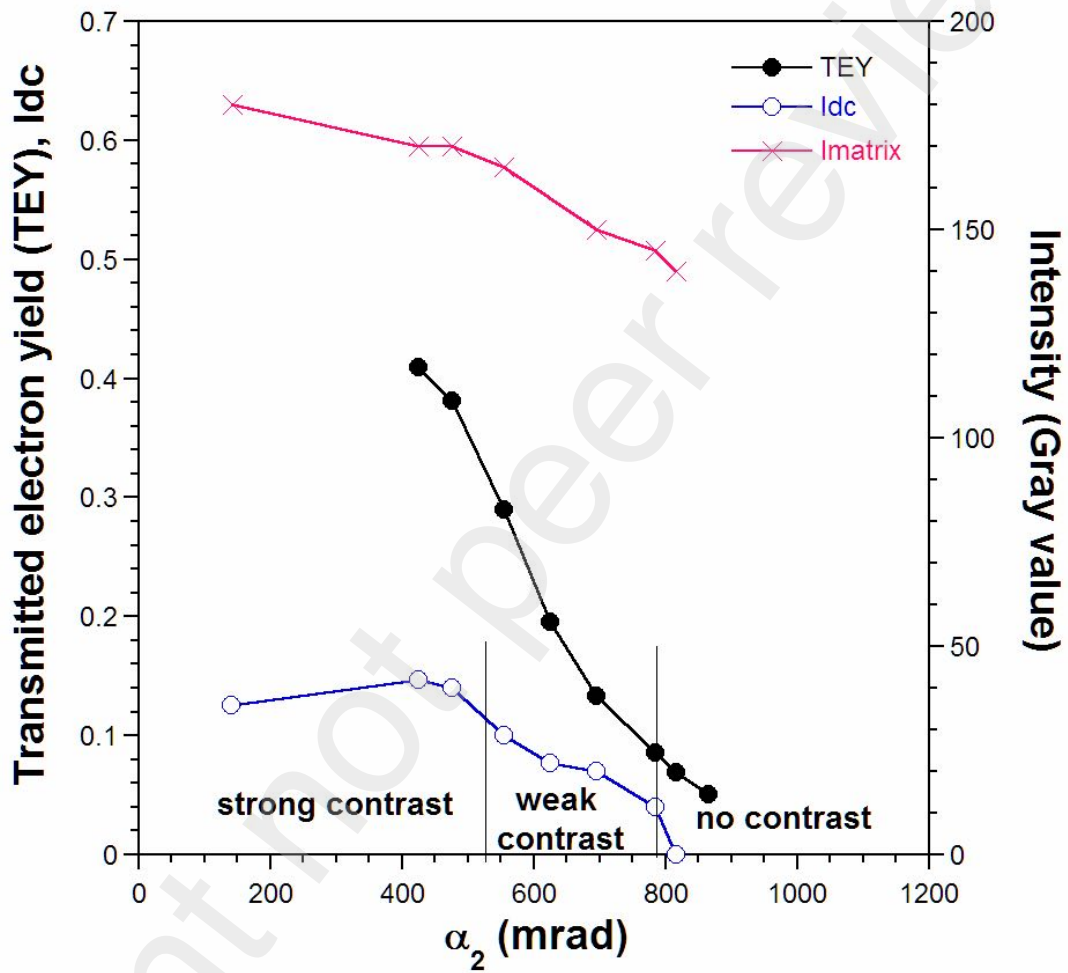


Figure 3. Variation of transmitted electron yield (TEY), dislocation contrast intensity, I_{dc} , and intensity of the t-FSE signal of the matrix, I_{matrix} , as a function of maximum collection angle, α_2 .

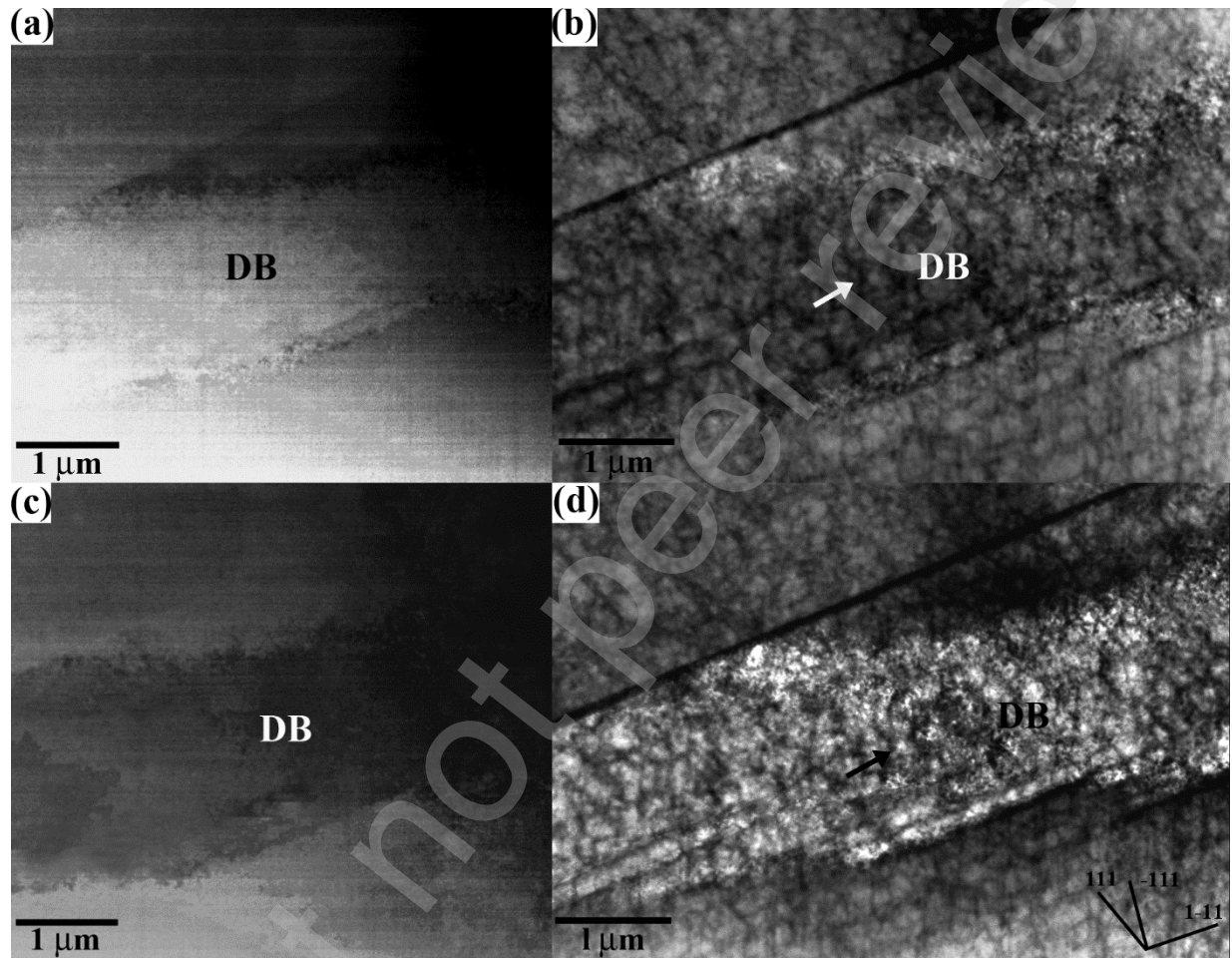


Figure 4. Influence of the channeling conditions on the ECC images (a, c) and (BF) t-FSE images of the dislocation configuration of a deformation band structure of a Fe-30Mn-6.5Al-0.3C alloy deformed at $-196\text{ }^{\circ}\text{C}$. The ECC/(BF) t-FSE images were taken under two-beam conditions using $g(2\ 4\ 0)$. (a, b): $w < 0$ conditions. (c, d): $w > 0$ conditions. DB: Deformation band.

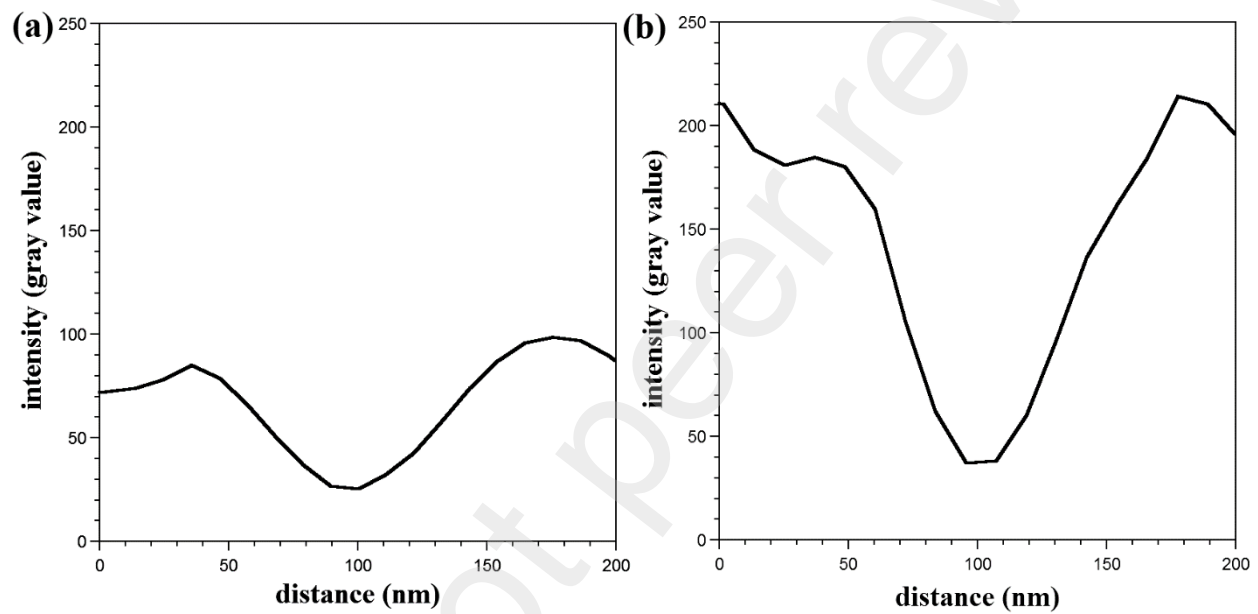


Figure 5. Intensity profiles of the t-FSE signal measured across the dislocation configuration indicated in Fig. 4. (a): $w < 0$ conditions. (b): $w > 0$ conditions.

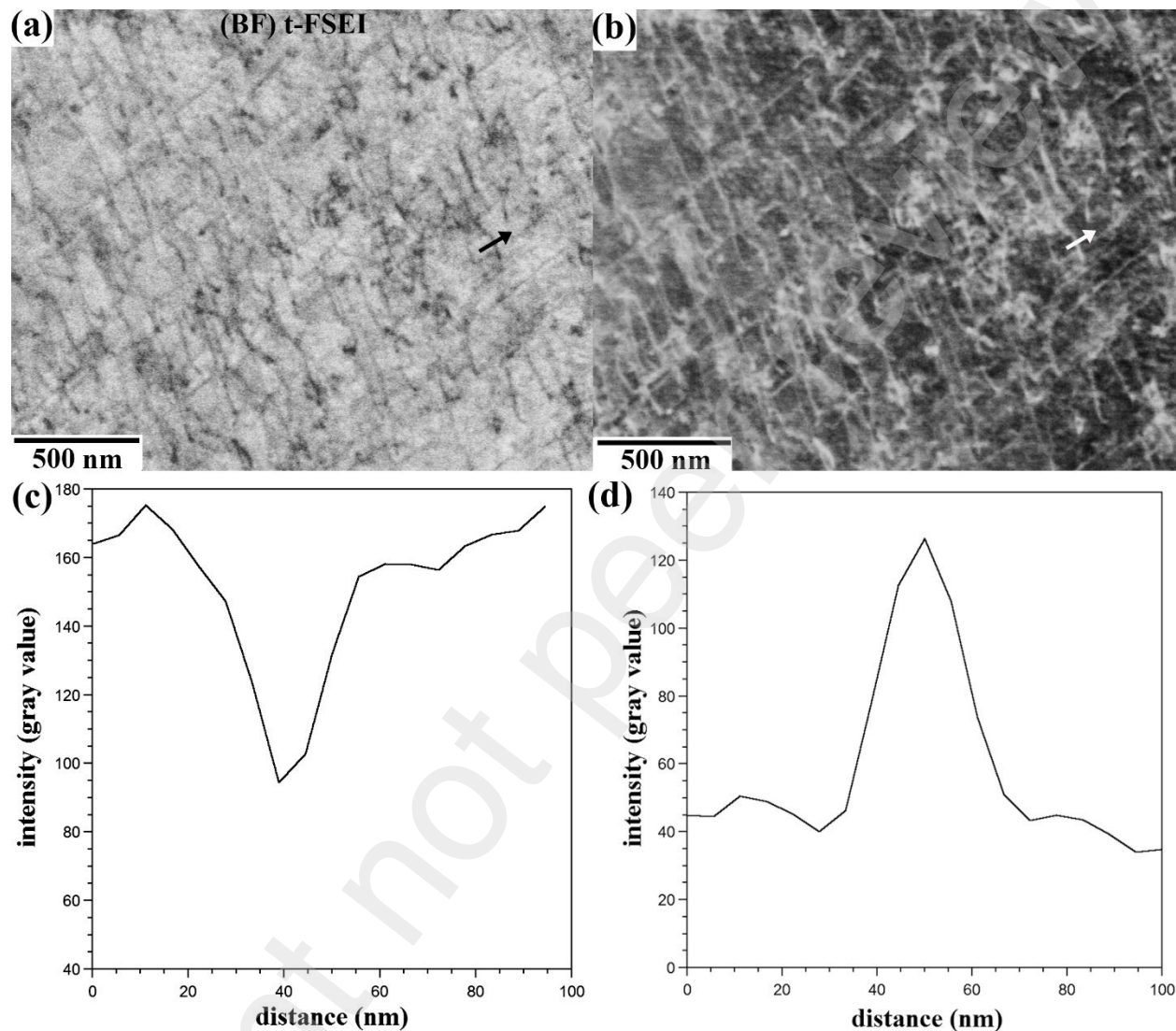


Figure 6. (BF) t-FSEI image (a) and ECC image (b) of the dislocation configuration in the interior of a α' martensite plate taken under the same two-beam diffraction conditions using the diffraction vector $(-2\ 1\ 1)$ with $w > 0$. (c, d): Intensity profiles across the dislocation line indicated by an arrow in (a) and (b).

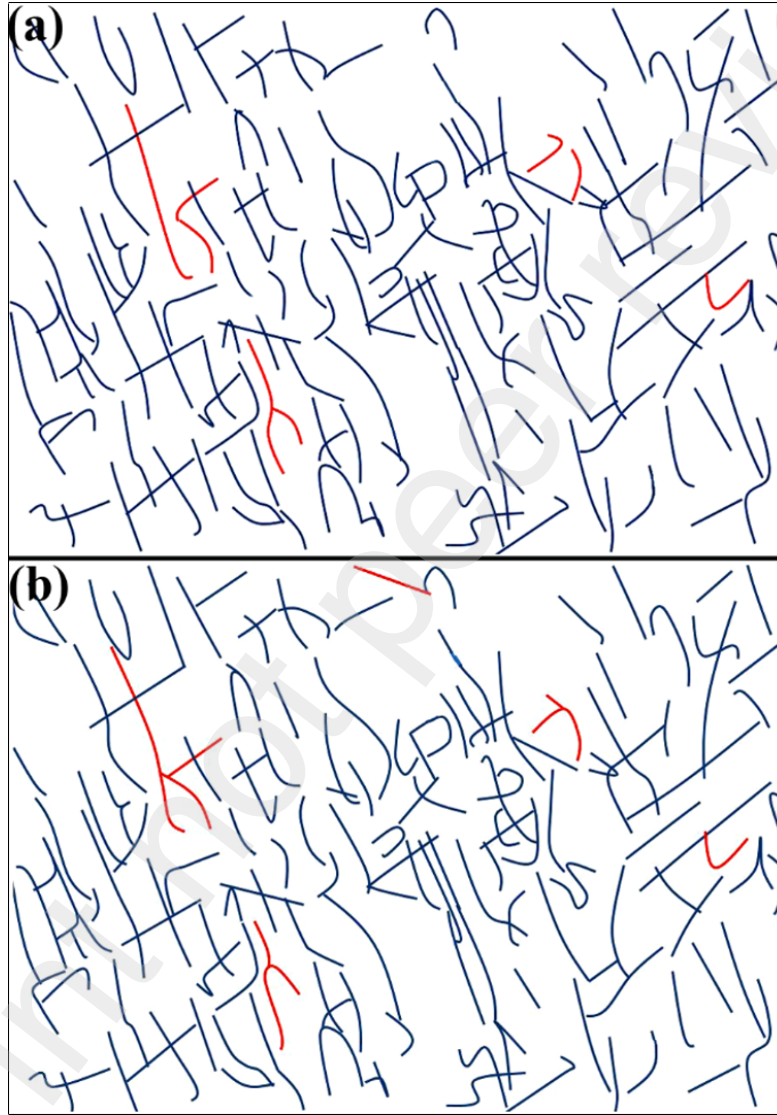


Figure 7. Analysis of the visible dislocation lines imaged in Fig. 4. (a): (BF) t-FSEI; (b): ECCI. Blue lines correspond to dislocation lines showing the same configuration imaged in both imaging modes. Red lines correspond to dislocation lines with a different imaged dislocation configuration.

Preprint not peer reviewed